A Control-Oriented Spatially Resolved Thermal Model of the Three-Way-Catalyst

2021-01-0597

A Control-Oriented Spatially Resolved Thermal Model of the Three-Way-Catalyst

Jonathan Lock, Kristoffer Clasén, Jonas Sjöblom, Tomas McKelvey

Abstract

The three-way-catalyst (TWC) is an essential part of the exhaust aftertreatment system in spark-ignited powertrains, converting nearly all toxic emissions to harmless gasses. The TWC's conversion efficiency is significantly temperature-dependent, and cold-starts can be the dominating source of emissions for vehicles with frequent start/stops (e.g. hybrid vehicles). In this paper we develop a thermal TWC model and calibrate it with experimental data. Due to the few number of state variables the model is well suited for fast offline simulation as well as subsequent on-line control, for instance using non-linear state-feedback or explicit MPC. Using the model could allow an on-line controller to more optimally adjust the engine ignition timing, the power in an electric catalyst pre-heater, and/or the power split ratio in a hybrid vehicle when the catalyst is not completely hot. The model uses a physics-based approach and resolves both axial and radial temperature gradients, allowing for the thermal transients seen during heat-up to be represented far more accurately than conventional scalar (i.e. lumped-temperature) real-time models. Furthermore, we also use a physics-based chemical kinetics reaction model for computing the exothermic heat of reaction and emission conversion rate which is temperature and residence-time-dependent. We have performed an experimental campaign with a standard spark-ignited engine and a commercial TWC, where we measured steady-state operation and cold-start transient behavior. This experimental data allowed us to tune the model, where we found excellent matching between the measured and modeled tailpipe emissions. Modeling the radial temperature gradient improved the relative accuracy of the conversion efficiency by 15%, and simulations indicate the potential for an absolute improvement by 15 percentage points for some cases. Furthermore, the modeled TWC temperature evolution for a cold-start was typically within ±10°C of the measured temperature (with a maximal deviation of 20°C). The proposed model thus bridges a gap between heuristic models suited for on-line control and accurate models for slower off-line simulation.

Introduction

The three way catalyst (TWC) is an essential part of the powertrain in virtually all spark-ignited (SI) automotive vehicles, significantly reducing the level of harmful emissions and keeping them below legislated limits. These emissions are generated by combustion processes in the engine, primarily consisting of carbon monoxide (CO), nitrogen oxides ($\mathrm{NO_x}$), and residual unburnt hydrocarbons (THC). In normal operation virtually all of the generated emissions are converted to non-toxic carbon dioxide ($\mathrm{CO_2}$), nitrogen gas ($\mathrm{N_2}$) and water ($\mathrm{H_2O}$) [1, 2]. In order to reach a high conversion ratio the TWC must be sufficiently warmed up by the engine exhaust, typically to at least 250–350°C. However, when a cold vehicle is started there is a short period, on the order of 10–30 seconds, where the TWC is not sufficiently warm to convert the exhaust emissions. This gives rise to a high level of tailpipe emissions, and for many regulatory test procedures these cold-start emissions are responsible for 60–80% of the emissions generated from an entire test (which are for comparison on the order of 30 minutes) [2].

Methods for reducing cold-start emissions have been studied extensively from several different perspectives, including TWC design methods that reduce the cold-start time [3], additional hardware that can pre-heat the TWC before starting the engine [4], and control schemes that control the engine's operation to reduce the generated emissions and/or heat the TWC more quickly [2, 5, 6, 7, 8]. One shared requirement for making a good design choice for all these tasks is a sufficiently accurate cold-start thermal model of the TWC. Ideally, a model should be able to predict both the spatially varying thermal dynamics and the conversion efficiency of the TWC to a sufficiently accurate degree. Naturally, more complex models allow for a higher degree of accuracy (for instance, a full 3D model), while simpler models are computationally faster.

In this paper we introduce and experimentally study a physics-based thermal TWC model that is both computationally fast enough to be used for on-line control methods, while simultaneously using a kinetic reaction model for emission species conversion and resolving both axial and radial temperature gradients. This is a significant improvement over many other numerically fast methods, which use simpler heuristics for emission conversion and/or assume a constant temperature profile in the TWC. Furthermore, the model allows for adjusting the number of axial and radial segments in order to tune the computational complexity to the available processing power. Ultimately, the model allows for more accurately simulating the behavior of the TWC, both for off-line applications that must be numerically fast as well as on-line control methods with limited computational capacity. For instance, an on-line controller could use the presented TWC model in combination with a model-based control method to balance emissions and fuel consumption by controlling the engine's ignition timing, an auxiliary catalyst heater, gear selection, and/or power split in the case of a hybrid vehicle. Similarly, off-line tuning of heuristic cold-start strategies is typically time-consuming when done by experimental test-bench studies or numerically slow simulations. The time needed to tune a heuristic controller could thus be reduced by instead simulating the TWC behavior with the presented model.

In this paper we will first give a brief overview of existing models and highlight their strengths, weaknesses, and possible applications. Following this we introduce and define the model, after which we

describe the experimental setup used to tune it. Finally, we compare the experimental data and the predictions from the model.

Literature survey

Many authors have considered the problem of modeling a TWC in a manner that is amenable to on-line control or very fast simulation. These models can generally be categorized by how they trade off accuracy and computational demand as well as which sources of dynamics the models choose to include.

The computationally fastest models typically assume one (scalar) TWC temperature that is influenced by the exhaust emissions and use a suitable function for determining the temperature-dependent conversion efficiency. One example of this is [9], which assumes a scalar TWC temperature whose state evolution is linearly influenced by the engine exhaust gas temperature, ambient temperature, and converted emission species. They further use the $\arctan$ function to approximate the temperature-dependence of the reactions occurring in the TWC. Finally, they use a dynamic programming (DP) method to solve an optimal control problem, which could be implemented as an on-line controller. See also [5, 6, 10] for similar (scalar TWC temperature) approaches.

Some authors chose to improve the accuracy of the TWC model by also modeling a TWC phenomenon wherein oxygen is absorbed and released from the TWC. The stored oxygen content influences the TWC's ability to remove emissions, where CO and THC are more efficiently oxidized when there is an overabundance of stored oxygen in the TWC, while $\mathrm{NO_x}$ is more efficiently converted when the oxygen content is low. For instance, [11] uses two state variables, one to store the TWC temperature similarly to the previous authors, and one to store the total stored oxygen in the TWC. This addition results in a model that more accurately captures the behavior of the TWC during phases where the air-fuel-ratio, often referred to as *lambda*, deviates from a stoichiometric condition. This occurs most prominently during fuel-cut operation, where the engine motors without any fuel injection, but also occurs during a short interval when the engine speed and load is changed [12, p. 69], as well as to a lesser extent during normal operation where lambda is periodically switched between slightly-rich and slightly-lean in order to improve the net TWC conversion efficiency [13]. A significant excursion from stoichiometric operation (i.e. beyond the ordinary rich/lean switching scheme) is typically handled by running the TWC at slightly rich or lean in order to bring the average lambda back to stoichiometry, and is crucial in order to maintain a high conversion efficiency.

One common approach of further improving model accuracy is by using a heterogeneous TWC model. Most commonly this is done by using a model that can represent varying TWC temperatures and/or stored oxygen. As the TWC is typically constructed with hundreds of identical parallel channels [1, p. 650], one might choose to assume that the gas flow, composition, and temperature is identical for all channels. By using this *single-channel approximation* our modeling focus can be directed to studying the behavior in one channel in isolation, after which we can compute the total TWC behavior via scaling by the number of channels. As each single channel is long and narrow one obvious method is to divide each channel into separate axial slices and then allow each slice to take on its own temperature and/or stored oxygen (e.g. [14, 15, 16], where temperature is axially resolved). Ultimately this allows for capturing transient behavior in the TWC, such as a cold-start, where the front of the TWC is typically several hundreds of degrees warmer than the rear.

The most practically significant drawback with more complex models is their increased computational demand. In particular, on-line control systems intended for native vehicle implementation are typically highly computationally limited, and any controller must be of low numerical complexity. There are several different approaches that can be used, ranging from using optimal control strategies as an inspiration for heuristic controllers [14], to more computationally expensive methods, for instance based on Pontryagin's Maximum Principle [15], while others primarily target simulation using hardware much more powerful than that found in vehicles [16].

Several powerful on-line control methods, e.g. nonlinear state feedback and some explicit MPC variants, can be implemented for nearly any practically relevant model complexity (nonlinear, non-convex, and non-differentiable) while being very computationally inexpensive to run on-line. These methods are computationally inexpensive as the model is never evaluated in the real-time controller. Instead, the control signal is generated by referring to a pre-computed look-up-table [17, 18], i.e. the optimal control can be computed by an interpolation operation (taking on the order of 5–10 CPU instructions) in the case of nonlinear state feedback, and a region identification and function evaluation step in the case of explicit MPC. However, these methods are limited by a computational complexity that scales very poorly (exponentially) with the number of state variables. This applies both to the off-line phase with respect to the computational demand of generating the model-derived look-up-table, as well as during the on-line phase with respect to memory requirements (as well as computational demand in some explicit MPC cases). This motivates a model that has a limited number of state variables, but may otherwise (within reasonable limits) be complex and nonlinear. Note that there exist on-line control methods that do not place as large demands on the number of state variables (e.g. linear programming methods, which scale polynomially with the number of state variables). However, these methods instead limit the complexity of the model dynamics, and can require them to be e.g. linear, convex in cost, and so on. In this paper we take the approach of limiting the number of state variables while allowing the dynamics to be nonlinear, which in turn makes for instance DP-based methods an attractive choice for subsequent simulation or controller generation.

Our goal with this paper is to develop an efficient TWC model suited for cold-starts, whose temperature evolution is driven by the time-evolution of the combustion engine's exhaust gas composition, temperature, and mass-flow. Our model primarily captures axial temperature variations as well as to some extent radial temperature variations, which we can view as using the axially-sliced single-channel approximation while also allowing the temperature of each channel to vary based on its radial position in the TWC. Given this goal and the limit on the number of state variables, it is natural to use a nested controller structure. For instance, an inner control loop to regulate the engine's lambda with a goal to maintain the correct stored oxygen, in concert with an outer control loop to regulate the engine's operating point (e.g. ignition timing, speed, and torque) with a goal to regulate the TWC temperature. Our model is therefore primarily designed for use as a supervisory controller, and assumes a lambda controller is already implemented. Note that since the behavior of the physical TWC depends on the lambda-controller, then a tuned thermal TWC model is also only valid for a given lambda-controller (i.e. it must be re-tuned if the lambda-controller is modified).

The presented model is to our knowledge novel in the sense that it uses a first-principles approach for both thermal conduction and chemical kinetics in a control-oriented context, meaning that we can avoid the use of heuristics to describe the thermal and chemical behavior. Furthermore, the model is configurable in the axial and radial resolution, allowing for balancing the model's accuracy and computational demand to the target application.

TWC model

In this section we will present the TWC model, which resolves both axial and radial temperature dynamics, uses a first-principles model for thermal conduction and exhaust gas species conversion reactions, and is easy to tune to experimental data.

In principle, the model is a nonlinear ordinary differential equation,

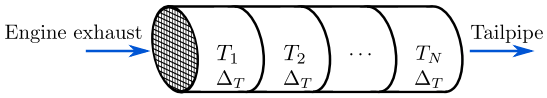

Figure 1: Axially and radially discretized TWC with state variable $\bar{T} = [T_1, T_2, \ldots, T_N, \Delta_T]$.

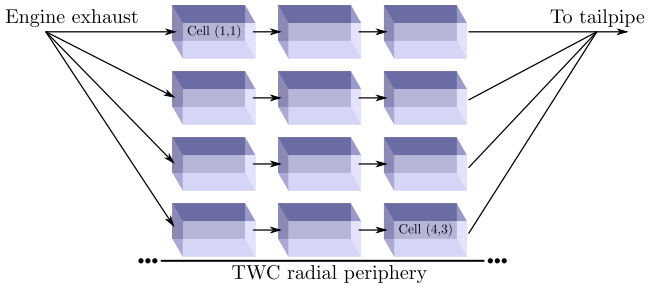

Figure 2: Fully thermally resolved TWC, here shown for $M = 4$, $N = 3$. Arrows show the exhaust gas flow through the different cells in the model.

where the temperature derivative depends on the current temperature and incoming gas properties. For ease of understanding we will introduce the model in a constructive manner, similar to an algorithmic implementation, divided into the following parts:

1. For given state variable values (which inherently only encode the TWC temperature at a few positions) a densely-sampled representation of the TWC's temperature distribution is generated where the radial resolution is significantly increased.
2. Once the dense temperature distribution is known, the properties of the gas entering the TWC are used to determine the outgoing gas properties and thermal flux in the TWC.
3. For a given thermal flux, the densely-sampled representation is converted to the time-derivative of the low-dimensional state variables.

Each of the above phases are defined in the following sections.

Generating the full temperature distribution

Figure 1 illustrates a typical cylindrical TWC monolith, which we have axially divided into N equally long slices. Each slice, n, has an associated state variable T_n that corresponds to the radially central temperature. A final state variable, Δ_T, represents the difference in temperature between the radial center of each slice and its associated periphery, giving the total state vector

$$\bar{T} = [T_1, T_2, \ldots, T_N, \Delta_T]. \tag{1}$$

Note that Δ_T is *not* axially resolved, i.e. the difference in temperature between the radial center and periphery of each slice is assumed constant throughout the entire TWC. This assumption is made in order to reduce the number of state variables.

In the first model step, we construct the full representation of the TWC temperature by increasing the radial resolution. An illustration of the full TWC model is shown in Figure 2, which consists of the same equally long N axial slices represented in the state vector, but is also extended radially with M evenly spaced elements. This gives a total of $N \cdot M$ *cells*, where each cell can be viewed as a small reactor with homogeneous temperature. Cells $(1, n)$ correspond to the radially centermost parts of the TWC, while cells (M, n) correspond to the radially outermost parts of the TWC. We naturally assume that

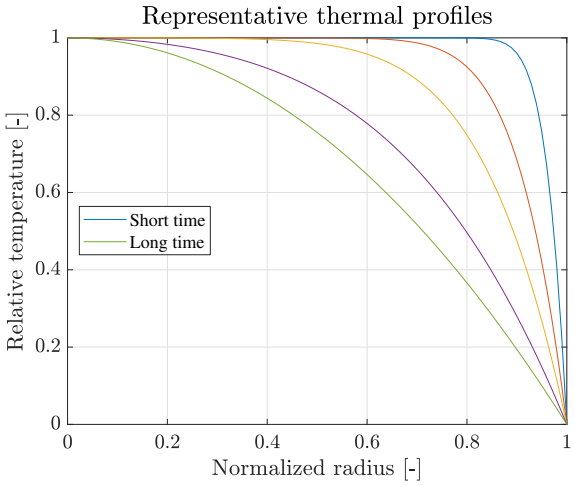

Figure 3: Representative solutions to the transient heat equation for varying times t. The shown solution's temperatures have been normalized to the range $[0, 1]$. With this normalization, the solution at radii $[0, 1)$ starts off at unit relative temperature, and as time progresses gradually approaches the closer-to linear distribution.

gas flows from one given axial position to its successor, without any radial transport between cells (as indicated by the arrows in Figure 2), i.e. we assume there is no gas diffusion between neighboring channels in the TWC. Cells $([1 \ldots M], 1)$ are fed with engine exhaust, cell $(m, n+1)$ is fed with the output of cell (m, n), and the output from cells $([1 \ldots M], N)$ are combined to form the total tailpipe exhaust. Note that as the TWC is circular, cells nearer the periphery have a larger associated open frontal area. We compensate for this by assuming a constant gas flow-rate, and weight the incoming massflow relative to each cell's relative area. Letting $\dot{m}_{\text{eng ex}}$ be the total massflow from the engine, the flow into each cell is then

$$\dot{m}_{m,1} = \frac{m^2 - (m-1)^2}{M^2} \cdot \dot{m}_{\text{eng ex}} \tag{2}$$

$$\dot{m}_{m,n+1} = \dot{m}_{m,n}. \tag{3}$$

In essence, we can view the full TWC model as consisting of M parallel single-channel models, each of which consists of N sections with different temperatures, and whose incoming massflow is proportional to its associated frontal area.

Each cell is assigned a temperature as follows:

- cells $(1, 1)$ through $(1, N)$ are assigned temperatures T_1 through T_N respectively (i.e. the radially centermost temperature),
- cells $(M, 1)$ through (M, N) are assigned temperatures $T_1 + \Delta T$ through $T_N + \Delta T$ respectively, (i.e. the radially outermost temperature), and
- the remaining cells, $(2, 1)$ through $(M-1, N)$, are assigned temperatures following a physics-based interpolation scheme described below.

Radial temperature profile

The radial temperature distribution (i.e. the temperature profile between the radial center and periphery) in the physical TWC varies depending on the properties of the incoming gas, and by extension the operating point of the combustion engine.

We have chosen to model the true radial temperature profile as a solution to the heat equation. More specifically, we solve the transient

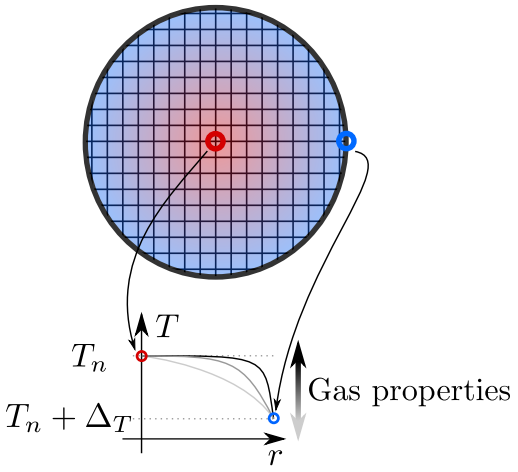

Figure 4: Each axial slice is assigned a radial temperature distribution that depends on the properties of the incoming exhaust gas. The radially centermost temperature (T_n) and radially outermost temperature ($T_n + \Delta_T$) in combination with the operating point is used to construct the radially-varying temperature distribution.

heat equation in a flat circular plate with radius R and homogeneous initial temperature $\hat{T}(r) = 0,\ r = [0, R]$ (note that despite the similar notation, $\hat{T}$ has no direct relation to the model state vector $\bar{T}$ or the axial slices T_n). Furthermore, we apply the boundary condition $\hat{T}(R) = 0$ at the periphery (i.e. a Dirichlet boundary condition), and assume the bulk of the plate develops a constant and homogeneous power (analogous to the energy delivered by the incoming gas to a given axial TWC slice). This is a textbook problem (e.g. [19, p. 148]) with a well-known solution that can be expressed as a Fourier-Bessel series. We can easily numerically solve this problem over time and along the plate's radius (for instance using MATLAB's `pdepe` function), generating the radially-varying time-evolution of the plate's temperature. We show normalized solutions, i.e. where $\hat{T}$ is offset and scaled so that $\hat{T}(0) = 1$ and $\hat{T}(R) = 0$, for some representative time instances in Figure 3 for $R = 1$.

In this paper we select the modeled TWC temperature profile at any given time (i.e. which profile we select from Figure 3) based on the engine's current operating point, as indicated in Figure 4, and we will return to the specific method for choosing a profile in the experimental results section. Ultimately, this gives an easily implemented interpolation method for cells $(2, 1)$ through $(M - 1, N)$ that matches the temperatures at the radial center and periphery, represented by $T_1, \ldots, T_N$ and $T_1 + \Delta_T, \ldots, T_N + \Delta_T$ respectively. The scheme is physically motivated, capturing the essence of the radial thermal conduction and incoming power from gas convection and exothermic heat of reaction.

Chemical kinetic model

Though the total set of reactions occurring in the TWC are highly complex and involve many different compounds, there are fewer components that contribute to the legislated emissions and significant heat generation. We therefore are only interested in the following net reactions (adapted from [11, 20])

$$2\,CO + O_2 \longrightarrow 2\,CO_2 \tag{4}$$
$$2\,NO + 2\,CO \longrightarrow N_2 + 2\,CO_2 \tag{5}$$
$$2\,NO_2 \longrightarrow N_2 + 2\,O_2 \tag{6}$$
$$2\,C_3H_6 + 9\,O_2 \longrightarrow 6\,CO_2 + 6\,H_2O \tag{7}$$
$$C_3H_8 + 5\,O_2 \longrightarrow 3\,CO_2 + 4\,H_2O. \tag{8}$$

Typically, engine-out nitrogen oxides and hydrocarbon emissions are lumped together [1, pp. 572, 597], and we thus categorize the the emission species as carbon monoxide (CO), nitrogen oxides (NO and NO_2), and hydrocarbons (C_3H_6 and C_3H_8). By [1, p. 578] we assume a constant molar ratio of 99:1 for NO to NO_2 (a similar ratio was found in our experimental tests). Similarly, by [21] and [22] we choose to assume a a 3:1 ratio for C_3H_6 to C_3H_8. For convenience, we will refer to these lumped emissions as NO_x and THC respectively.

We use an Arrhenius expression to model the reaction rate $k^s_{n,m}$ of a given emission species s (i.e. CO, NO_x, and THC) in any given cell n, m as

$$k^s_{n,m} = A^s e^{\frac{-E^s_a}{RT_{n,m}}} \tag{9}$$

where R is the ideal gas constant, $T_{n,m}$ is the temperature of cell n, m, E^s_a is the activation energy of emission species s, and A^s is the apparent pre-exponential factor for species s (which is dependent on the cell's volume). Using the notation $y^s_{n,m}$ to indicate the mole fraction of emission species s, we model the evolution of the mole fraction as

$$\frac{\mathrm{d}y^s_{n,m}}{\mathrm{d}t} = -k^s_{n,m} y^s_{n,m}. \tag{10}$$

For a typical TWC, the gas residence time in each slice is short enough for the temperature to be close-to constant, which we will now motivate. In [6, p. 64], the authors find that the gas residence time in the *entire* TWC is typically in the range of 0.05–0.1 s, e.g. with 4 axial slices the residence time in each slice is typically 12.5–25 ms. Furthermore, [6, p. 66] also finds that the typical temperature time-derivative in the TWC during a cold-start is on the order of 10°C/s (this is similar to our findings, which we will see later). Ultimately this implies that the temperature in a given axial slice changes by approximately 0.1–0.25°C during the time the gas is in each slice, which we view as insignificant.

Using the constant-temperature approximation, (10) has the explicit solution

$$y^s_{n,m}(t_r) = y^s_{n,m}(0) \cdot e^{-k^s_{n,m} t_r} \tag{11}$$

for a residence time t_r. We will assume a simple plug flow reactor model (i.e. no axial mixing), which gives

$$t_r = \frac{V_{\text{slice}}}{\nu} \tag{12}$$

where V_{slice} is the volume of each axial slice and ν is the volumetric gas flow rate. We generate the slice volume as

$$V_{\text{slice}} = \frac{V_{\text{TWC}}}{N}, \tag{13}$$

where V_{TWC} is the gas volume of the entire TWC. We further estimate ν as

$$\nu = \frac{\dot{m}_{\text{eng ex}}}{P/(R_{\text{specific}} T_{n,m})} \tag{14}$$

where P is the absolute pressure in the TWC (typically close to ambient pressure) and R_{specific} is the specific gas constant for the post-TWC ratio of N_2, CO_2, O_2, and H_2O we measured in our experimental trials during stoichiometric operation. We have chosen to use this specific gas constant as it is easily determined and the remaining gasses contribute minimally to R_{specific}.

Ultimately, using (9) through (14) gives a simple, but physics-based, model for the reactions occurring in the TWC that takes temperature, gas composition, and residence time into account. This implies that the model is suited for quasi-stationary combustion engine operation, where the engine-out exhaust temperature, emission species mole fraction, and massflow varies slowly with respect to the residence time. Though the model will not accurately capture the true behavior during engine transients, as gas at different positions in the TWC will

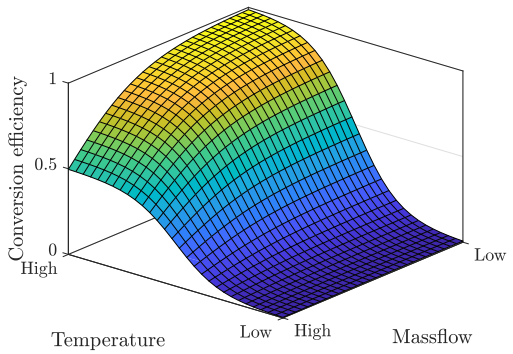

Figure 5: Representative conversion efficiency for a given emission species and cell, with maximal efficiency at low massflow (i.e. longer residence time) and high temperature.

have originated from the engine operated at different regimes, we hypothesize (but were not able to verify with the available measurement equipment) that the predicted TWC performance converges to the measured performance on a time scale that is comparable with the residence time in the TWC.

By (11), the massflow emitted from cell n, m is

$$\dot{m}^{s,\text{out}}_{n,m} = \dot{m}^{s,\text{in}}_{n,m} e^{-k^s_{n,m} t_r} \tag{15}$$

and, by the conservation of mass, the converted massflow is

$$\dot{m}^{s,\text{conv}}_{n,m} = \dot{m}^{s,\text{in}}_{n,m} - \dot{m}^{s,\text{out}}_{n,m}. \tag{16}$$

Furthermore, we define the conversion efficiency of each cell as

$$\eta^s_{n,m} = 1 - \frac{\dot{m}^{s,\text{out}}_{n,m}}{\dot{m}^{s,\text{in}}_{n,m}}. \tag{17}$$

A qualitative illustration of the conversion efficiency as a function of massflow and temperature is shown in Figure 5.

Finally, we model the tailpipe emission of species s as the sum of outputs from each element in the last axial segment, i.e.

$$\dot{m}^s_{\text{tp}} = \sum_{m=1}^{M} \dot{m}^s_{m,N}. \tag{18}$$

In order to determine the exothermic reaction power generated by the above reactions, we can compute the (temperature-dependent) heat of reaction for each mole of reactant species as

$$\mathrm{d}H_{\text{CO}} = H_{0,\text{CO}_2} - H_{0,\text{CO}} - 1/2 H_{0,\text{O}_2} \tag{19}$$
$$\mathrm{d}H_{\text{NO}} = 1/2 H_{0,\text{N}_2} + H_{0,\text{CO}_2} - H_{0,\text{NO}} - \mathrm{d}H_{\text{CO}} \tag{20}$$
$$\mathrm{d}H_{\text{NO}_2} = 1/2 H_{0,\text{N}_2} + H_{0,\text{O}_2} - H_{0,\text{NO}_2} \tag{21}$$
$$\mathrm{d}H_{\text{C}_3\text{H}_6} = 3H_{0,\text{CO}_2} + 3H_{0,\text{H}_2\text{O}} - H_{0,\text{C}_3\text{H}_6} - 9/2 H_{0,\text{O}_2} \tag{22}$$
$$\mathrm{d}H_{\text{C}_3\text{H}_8} = 3H_{0,\text{CO}_2} + 4H_{0,\text{H}_2\text{O}} - H_{0,\text{C}_3\text{H}_8} - 5H_{0,\text{O}_2}. \tag{23}$$

Note that we have neglected to indicate the temperature dependence of these above terms for brevity, but include the temperature dependence in the model by using the Shomate equation and reference constants given by the NIST available at `https://webbook.nist.gov/` . The heat of reaction for the lumped emission terms is then similarly given by the weighted average

$$\mathrm{d}H_{\text{NO}_\text{x}} = (99\mathrm{d}H_{\text{NO}} + \mathrm{d}H_{\text{NO}_2})/100 \tag{24}$$
$$\mathrm{d}H_{\text{THC}} = (3\mathrm{d}H_{\text{C}_3\text{H}_6} + \mathrm{d}H_{\text{C}_3\text{H}_8})/4. \tag{25}$$

Using (19), (24), and (25) the total temperature-dependent heat of reaction generated in each cell is given as

$$P_{n,m} = \dot{m}^{\text{CO,conv}}_{n,m} \cdot \mathrm{d}H_{\text{CO}} + \dot{m}^{\text{NO}_\text{x},\text{conv}}_{n,m} \cdot \mathrm{d}H_{\text{NO}_\text{x}} + \dot{m}^{\text{THC,conv}}_{n,m} \cdot \mathrm{d}H_{\text{THC}}. \tag{26}$$

Generating the state vector derivative

In this stage, we use the previously computed converted massflow and associated exothermic reaction power per cell to generate the state vector derivative. Note that the state derivative is of size $N + 1$, i.e. the information encoded in the $N \cdot M$ cells is reduced to $N + 1$ dimensions. The state derivative is constructed from three different terms:

$$\frac{\mathrm{d}\bar{T}}{\mathrm{d}t} = \bar{T}_{\text{cond}} + \bar{T}_{\text{exo}} + \bar{T}_{\text{convect}}. \tag{27}$$

Here, $\bar{T}_{\text{cond}}$, $\bar{T}_{\text{exo}}$, and $\bar{T}_{\text{convect}}$ correspond to bulk thermal conduction, exothermic reaction power, and the convective power from the incoming gasses. Theses terms are in turn defined as follows.

Thermal conduction

We model thermal conduction in the TWC, $\bar{T}_{\text{cond}}$, both axially and radially as

$$\bar{T}_{\text{cond}} = \frac{1}{\tau_{\text{ax}}} \begin{bmatrix} T_2 - T_1 \\ \vdots \\ T_{n-1} + T_{n+1} - 2T_n \\ \vdots \\ T_{N-1} - T_N \\ 0 \end{bmatrix} \tag{28}$$

$$+ \frac{1}{\tau_{\text{ra}}} \begin{bmatrix} \Delta_T \\ \vdots \\ \Delta_T \\ -\Delta_T \end{bmatrix} \tag{29}$$

$$+ \frac{1}{\tau_{\text{amb}}} \begin{bmatrix} 0 \\ \vdots \\ 0 \\ T_{\text{amb}} - \frac{1}{N}\sum_{n=1}^{N}(T_n + \Delta_T) \end{bmatrix}, \tag{30}$$

where τ_{ax}, τ_{ra}, and τ_{amb} are scalar tuning parameters that capture the net axial, radial, and ambient thermal resistance respectively and T_{amb} is a given ambient temperature. Note that $\bar{T}_{\text{cond}}$ is given as the sum of three terms, corresponding to axial conduction (28), radial conduction (29), and heat transfer to the ambient environment (30) respectively. Each of these three terms are motivated by the 1-dimensional heat equation [19]. In particular, note that in (30) $\frac{\mathrm{d}\Delta_T}{\mathrm{d}t}$ is given by the difference in temperature between the ambient and *mean* peripheral temperature. This is ultimately due to our choice of assuming a scalar core/periphery temperature difference, i.e. one that is identical for all axial slices.

Exothermic terms

We introduce

$$P_{\text{ctr},n} = \sum_{m=1}^{M} P_{n,m}(1 - \frac{m-1}{M-1}) \tag{31}$$

as the weighted exothermic reaction power associated with the radial center of the TWC for axial position n. Note that the term $\frac{m-1}{M-1}$ varies from 0 to 1 for m from 1 to M, i.e. a linear weighting. We have chosen this specific weighting as it matches our intuition in that exothermic power near the center of the fully resolved TWC should be assigned to the state variables corresponding to the axial center, and vice-versa for the periphery. However, this is only a first approximation and an optimal weighting might be different.

Similarly, we introduce

$$P_{\text{per},n} = \sum_{m=1}^{M} P_{n,m} \frac{m-1}{M-1} \tag{32}$$

as the weighted exothermic reaction power associated with the periphery of the TWC for axial position n. In essence, $P_{\text{ctr},n}$ and $P_{\text{per},n}$ collect the exothermic reaction power developed in each cell, weighting power near the center to $P_{\text{ctr},n}$ and power near the periphery to $P_{\text{per},n}$.

We can now define the state derivative terms due to the heat of reaction as

$$\bar{T}_{\text{exo}} = k_{\text{conv}} \begin{bmatrix} P_{\text{ctr},1} \\ \vdots \\ P_{\text{ctr},N} \\ \frac{1}{N}\sum_{n=1}^{N}(P_{\text{per},n} - P_{\text{ctr},n}) \end{bmatrix}, \tag{33}$$

where k_{conv} is a tuning parameter for the proportionality between heat of reaction and the temperature derivative, i.e capturing the heat capacity of the TWC. Note that if P_{ctr} and P_{per} are expressed in Watts and $\bar{T}_{\text{exo}}$ as K/s then k_{conv} will have units J/K. Finally, note that the last element of $\bar{T}_{\text{exo}}$ can be seen as the average difference in power between the radially central and peripheral exothermic reaction powers, which is thus proportional to $\frac{\mathrm{d}\Delta_T}{\mathrm{d}t}$.

Convective terms

We model the temperature derivative from convective terms driven by the incoming gas as

$$\bar{T}_{\text{convect}} = \frac{\dot{m}_{\text{eng ex}}}{\tau_{\text{convect}}} \begin{bmatrix} T_{\text{eng ex}} - T_1 \\ \vdots \\ T_{n-1} - T_n \\ \vdots \\ T_{N-1} - T_N \\ 0 \end{bmatrix} \tag{34}$$

where $T_{\text{eng ex}}$ is the temperature of the gas entering the TWC and τ_{convect} is a tuning parameter proportionality constant, capturing the the specific heat of the exhaust gas and the heat capacity of the TWC. Note that (34) implies that the gas leaving each given cell is assumed to have the same temperature as the cell itself, i.e. each cell can be viewed as a reactor that is long enough for the moving gas to attain the same temperature as the cell before leaving (motivated by [6, p. 62] for $N \leq [2, 5]$). Also, recall that the final element of $\bar{T}_{\text{convect}}$ stores the difference in temperature between the radially central and peripheral part, i.e. setting the final element of (34) to 0 implies radially uniform gas flow through the TWC.

Experimental setup

Engine

The engine setup consisted of a production Volvo Cars two liter in-line four-cylinder direct injected spark ignited turbocharged engine rated at 187 kW and 350 Nm, as listed in Table 1. The engine exhaust was connected to an exhaust aftertreatment system consisting of a TWC equipped with wide-band lambda sensors, 14 thermocouples, and five exhaust gas sampling locations, both measuring average and point source gas compositions. The engine was connected to an electrical dynamometer that regulated the engine speed and measured the delivered torque. A prototyping ECU was used to allow sampling and changing engine parameters.

An auxiliary air valve was added to the exhaust manifold, allowing for flushing the entire exhaust aftertreatment system with room-temperature air for the cold-start tests. Cutting all fuel to the engine (while pumping air through the engine) and flushing with auxiliary air allowed for rapidly cooling the exhaust aftertreatment system, taking approximately 5 minutes to cool the entire TWC to

Table 1: Engine properties.

Engine type	VEA Gen I, VEP4 MP
Number of cylinders	Four, in-line
Displaced volume	1969 cc
Bore/Stroke	82 mm/93.2 mm
Compression ratio	10.8:1
Valve train	DOHC, 16 valves
Intake camshaft	Variable 0-48° CA advance
Exhaust camshaft	Variable 0-30° CA retard
Ignition system	DCI, standard J-gap spark plugs
Fuel system/Injection pressure	DI/200 bar
Fuel	Gasoline RON95 E10
Start of injection	308-340 CAbTDCf
Boosting system	Turbocharger
Rated power/Rated torque	187 kW/350 Nm
Stoichiometric air/fuel ratio	14.01:1

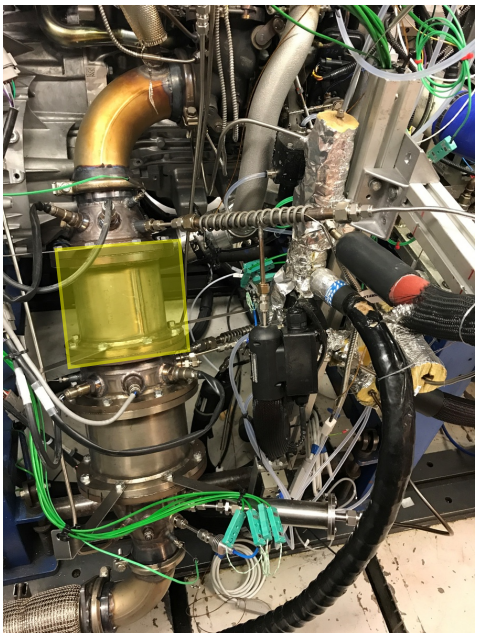

Figure 6: Experimental setup, TWC housing highlighted. Above the TWC is a 90°elbow. The turbocharger exhaust is just visible to the right of the elbow. Below the TWC is a GPF (not used in this experiment) and a flexible bellows.

under 100°C. The auxiliary airflow was kept small enough to avoid the turbo spooling up, which might cause an undesirable transient when resuming normal operation. During all normal engine operation the auxiliary air valve was kept closed in order to not alter the composition and temperature of the engine exhaust.

A photograph of the aftertreatment system is shown in Figure 6, with a schematic representation is shown in Figure 7 and a detailed view of the TWC in Figure 8. The schematic shows the engine exhaust and auxiliary cool-down air feed entering the turbo, which then proceeds through a 90°elbow, enters the TWC, and then is finally exhausted. Gas composition measurement points are located before and after the TWC which sample the average gas composition. An additional three sample points are located at the left, center, and right of the TWC, which allow sampling the local gas composition leaving a few TWC channels.

Data Acquisition

Data was sampled using two data acquisition systems. Emissions signals from instruments, fuel, and the dynamometer were sampled

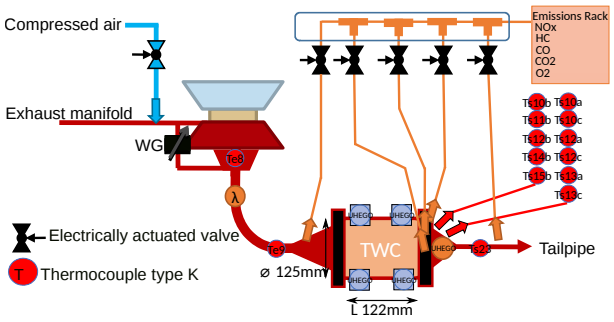

Figure 7: Schematic diagram of experimental setup.

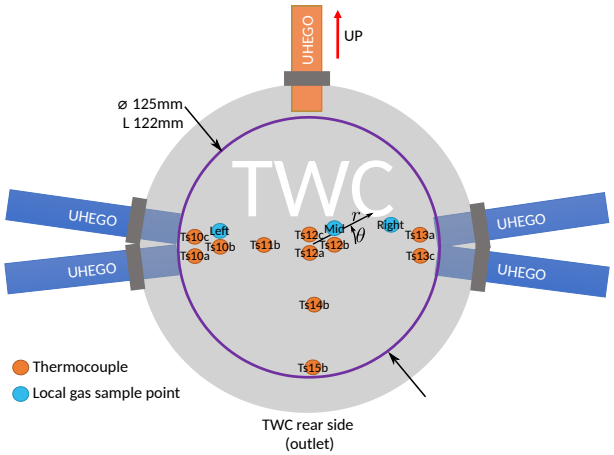

Figure 8: TWC instrumentation as seen from rear (outlet) side. Thermocouple locations indicated with orange, local gas sample points indicated with blue. See Table 2 for detailed thermocouple positioning.

Table 2: Thermocouple positioning. Depth indicates position of thermocouple relative to rear (outlet) of monolith. TWC length, diameter, and radius/azimuth reference as shown in Figure 8.

THERMOCOUPLE	RADIUS r [MM]	AZIMUTH θ [°]	DEPTH [MM]
Ts10a	61	180	-100
Ts10b	61	180	-60
Ts10c	61	180	-20
Ts11b	30	180	-60
Ts12a	0	0	-100
Ts12b	0	0	-60
Ts12c	0	0	-20
Ts13a	61	0	-100
Ts13c	61	0	-20
Ts14b	30	270	-60
Ts15b	61	270	-60

Table 3: Steady-state operating points. The load point at 3000 rpm, 8 bar BMEP, 1.05λ was not measured due to time constraints.

SPEED [RPM]	BMEP [BAR]	LAMBDA [-]
1000	2	0.95/1.00/1.05
1500	5	0.95/1.00/1.05
2000	15	0.95/1.00/1.05
3000	8	0.95/1.00

with a National Instruments DAQ and an associated LabVIEW program. Engine parameters such as temperatures, pressures, and target lambda were sampled using acquisition units connected via CAN to an ETAS-module. All temperatures were measured using type K thermocouples. Fuel flow mass was measured with a Coriolis meter. All parameters were sampled at a rate of 10 Hz.

Exhaust samples were extracted from five different locations (as indicated in Figure 7). Regardless of sample location, all were extracted via a heated hose (180°C), followed by a heated conditioning unit (190°C) with a heated filter and pump. Emissions concentrations were then analyzed by separate instruments. Total hydrocarbon concentration (THC) was measured using a flame ionization detector, NO_x concentrations using a chemiluminescence analyzer, and CO using a non-dispersive infrared detector. The propagation delay and axial dispersion in hoses and instruments was identified by generating a step in emissions (by disabling the fuel-cut signal as will be described in the cold-start experimental procedure). From this data we could compensate for the propagation delay as well as apply a first-order high-pass filter to mitigate some of the axial dispersion in the measured pre-catalyst emission data. This compensation was then applied to all other emission sampling locations, allowing for studying transient gas composition changes fairly well using an instrument rack primarily intended for steady-state analysis. Ultimately however, our experimental set-up only allowed for measuring emissions at any one given location at a time. We therefore chose to keep the engine in stationary operation in order to maximize the repeatability of the engine-out emissions, which was critical for generating an accurate estimate of the TWC's conversion efficiency.

Measurement procedure

The emission measurement equipment was calibrated before measurements using calibration gasses, and the engine was heated to its working temperature by running at a moderate load until the coolant temperature remained constant. Afterwards, we performed two different tests.

Steady-state analysis

The goal of this test was to identify the steady-state engine-out emissions and associated steady-state radial temperature distribution in the TWC for the engine operating points that can plausibly occur during a low- to medium-load cold-start. This was performed by statically running the engine and storing the steady-state values of all measured signals. The target lambda value was set swept between slightly rich, stoichiometric, and slightly lean in order to characterize the steady-state engine-out emissions[1]. This was then repeated for the operating points listed in Table 3.

[1]The conventional cold-start lambda-switching routine was not altered during this test, i.e. the instantaneous lambda value was automatically switched to slightly above and slightly below the target lambda. We only discuss the target (average) lambda here.

Cold-start thermal evolution

This goal of this test was to characterize the thermal evolution of the catalyst during a cold start. We performed this experiment for each emission sampling point by:

- bringing the engine to a moderate speed and torque (1500 RPM and 5 bar BMEP, giving a suitably long warm-up phase),
- disabling fuel injection (i.e. pumping air only) and opening the auxiliary air valve until the thermocouples in the TWC reported a temperature of under 100°C,
- first closing the auxiliary air valve and then enabling ordinary fuel injection until the TWC reached near-equilibrium temperature.

To capture the ordinary behavior of the engine during a cold-start, we ensured that the lambda control was run in open-loop, i.e. the narrowband lambda sensor after the TWC was not used to fine-tune the engine's air-fuel ratio. Instead, the ECU's conventional open-loop scheme was kept active during all tests, which periodically switches between lean and rich phases with $\lambda \approx \{0.98, 1.02\}$. This switching period is reduced as engine speed and torque increases, leading to poor lambda control at moderate loads and above. Due to this we kept the engine load fairly low during tests, at 1500 RPM and 5 bar BMEP.

Experimental results

Steady-state

The results from the steady-state experiment are listed in Table 4, showing the measured engine-out temperature, massflow, and emission concentration. The relative midway temperature

$$t_{\text{mid}} = \frac{\text{Ts11b} - \text{Ts10b}}{\text{Ts12b} - \text{Ts10b}},$$

indicates the relative temperature of thermocouple Ts11b (the axial and radial midpoint of the catalyst), where 0 corresponds to the temperature of the radial periphery (i.e. Ts10b) and 1 corresponds to the temperature of the radial center (i.e. Ts12b).

Cold-start thermal evolution

An illustration of the temperature evolution in the TWC is shown in Figure 9. It shows the radial and azimuth temperature evolution (Figure 9a) and the radially central and radially peripheral axial thermal evolution (Figure 9b) for the tested load step. Notably, Figure 9a indicates that there are no significant azimuth thermal variations (as Ts11b and Ts14b exhibit virtually identical trajectories), in turn indicating that the gas flow through the TWC is fairly evenly distributed azimuthally and that the radius of the 90°elbow after the turbocharger is sufficiently large for near-uniform flow. Furthermore, some radial variations are visible, as the radially outermost thermocouples (Ts10b, Ts15b) show a lower temperature after ≈ 100 s. Figure 9b shows a very significant axial thermal variation, with a clearly visible thermal front progressing over time from the incoming gas (Te9), to the front of the TWC (Ts10a/Ts12a), followed by the middle (Ts10b/Ts12b) and the rear (Ts10c/Ts12c) of the TWC, and finally the gas exiting the TWC (Ts23). Furthermore, the radial peripheral temperature is bears a close resemblance to the radially central temperature of each given axial slice. This motivates our choice of modeling the radially peripheral temperature as $T_n + \Delta_T$ (i.e. the peripheral temperature varies axially), in contrast to assuming a constant peripheral (canning) temperature. These results thus lend weight to our approach of modeling primarily axial, and to some extent radial, thermal variations.

An illustration of the net conversion efficiency of the TWC, defined as the ratio of the total converted mass to total incoming mass, is illustrated with dashed lines in the upper part of Figure 10. This figure was generated by using time-resolved emission data from two different sampling points, one before the TWC (i.e. measuring the total generated emissions) and one after the TWC (i.e. measuring the total remaining emissions). The figure illustrates that CO and $\mathrm{NO_x}$ reach light-off more quickly than THC, which is to be expected [1, p. 652]. Furthermore, we can reach a more fundamentally important conclusion; any attempt to characterize the entire TWC's conversion efficiency as a function of a single temperature during a thermal transient is bound to be limited in its accuracy. As Figure 9b shows, at for instance $t = 75$ s, the front of the catalyst is ≈ 375°C, while the rear is ≈ 125°C. We see a similar, albeit smaller, radial thermal difference in Figure 9a. Ultimately, this again motivates our modeling choice of a thermally resolved axi-radial model.

Model tuning

We utilized the experimental data in the previous section to tune the model constants. The tuning phase was divided into three different stages:

Radial temperature profile

By using the relative mid temperature, as found in the steady-state experiment and listed in Table 4, we uniquely determined the radial temperature profile associated with a given engine operating point. We followed the method described in the TWC model section, where we solved and normalized the heat equation solution over time. Afterwards, we selected the solution associated at a given time where the half-radius relative temperature was equal to the measured relative mid temperature t_{mid}.

Reaction rate parameters

The parameters E_a and A, as used in (9), were estimated using the cold-start experimental results. First, we assigned the time-evolution of the model's states to the measured thermal evolution (as shown in Figure 9). With our experimental data using three axial slices is most convenient, as we can generate $\bar{T} = [T_1, T_2, T_3, \Delta_T]$ directly by Ts12a, Ts12b, Ts12c, and Ts10b − Ts12b respectively. This explicitly gives the sample-evolution of the state vector $\bar{T}(k)$, where $k = 0, 1, 2, \ldots$ indicates the time-sample of the state vector, sampled at rate of 10 Hz. The radial temperature profile was estimated using $M = 15$ independent radial channels. We chose to use 15 radial channels as this is sufficiently large to resolve the most significant radial temperature distribution, as will be shown later.

For given E_a^s and A^s we computed the modeled tailpipe output emissions $\dot{m}_{\text{tp}}^s(k)$ using (9) through (18). Finally, we tuned E_a^s and A^s by solving the numerical optimization problem

$$\min \sum_k |\dot{m}_{\text{tp}}^s(k) - \dot{m}_{\text{tp,meas}}^s(k)|^2 \tag{35}$$

for all measured samples (as shown in Figure 9), and where $\dot{m}_{\text{tp,meas}}^s(k)$ was the measured tailpipe emissions of each emission species.

We solved (35) using the `patternsearch` optimization tool in MATLAB (a gradient-free direct-search method bearing some similarity to the Nelder-Mead method), which gave good matching between the measured and simulated output emissions, as shown in Figure 10. Note that the first 5 – 10 seconds of experimental data is of lower accuracy, particularly for THC, as the sharpening filter used could not completely compensate for the axial dispersion in the sampling lines and pump leading to the measurement equipment. This otherwise very good match indicates our choice of using a Arrhenius expression (9) and a first-order rate equation (10) can accurately approximate the true reactions in the TWC. The numerically

Table 4: Steady-state engine-out temperature, massflow, relative gas composition, and TWC midway temperature.

SPEED [RPM]	BMEP [BAR]	LAMBDA [-]	TEMPERATURE [°C]	MASSFLOW [G/S]	CO [PPM]	NOX [PPM]	THC [PPM]	t_{MID} [-]
1000	2	0.95	356	5.81	14500	151	586	0.723
		1.00	368	5.95	4660	183	470	0.787
		1.05	361	6.13	1370	325	405	0.757
2000	15	0.95	755	56.9	16000	1660	319	0.797
		1.00	755	55.6	3920	2720	204	0.815
		1.05	744	57.1	1270	3070	117	0.816
3000	8	0.95	812	50.0	15600	1050	293	0.912
		1.00	860	53.3	2140	1530	11.3	0.858
1500	5	0.95	583	16.3	14900	357	384	0.919
		1.00	623	17.6	4130	529	225	0.940
		1.05	642	19.7	943	782	59.7	0.983

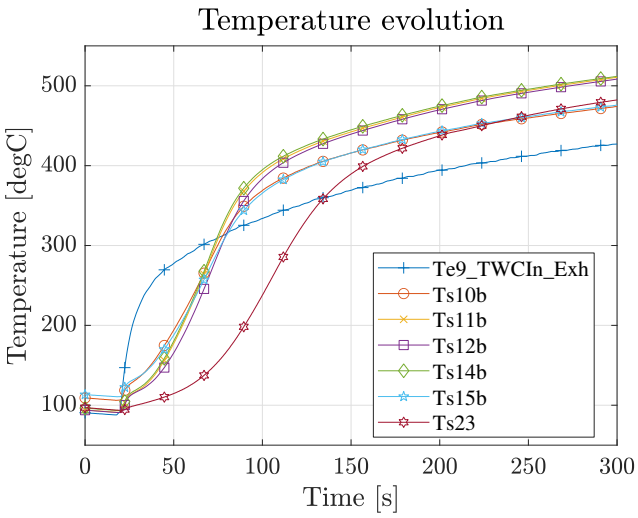

(a) Radial and azimuthal temperature evolution of axially central slice. The radially central portions of the TWC heats earlier (Ts11b-Ts14b) than the radially outer parts (Ts10b, Ts15b). No noticeable azimuth variation.

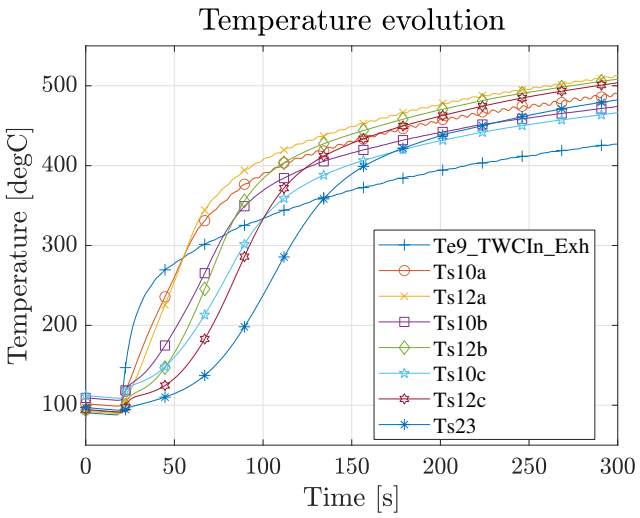

(b) Axial temperature variation of radially central and radially peripheral sections. The sensors closest to the engine exhaust (Ts10a, Ts12a) heat up first, while sensors successively further back (Ts10b/Ts12b, and Ts10c/Ts12c) heat up after each other. Sensors of the same axial position (Ts12a and Ts10a, Ts12b and Ts10b, Ts12c and Ts10c) show a strong interdependence, motivating our modelling approximation of Δ_T being constant axially along the TWC.

Figure 9: Temperature evolution of TWC. Sensor locations as shown in Figure 7 and Figure 8.

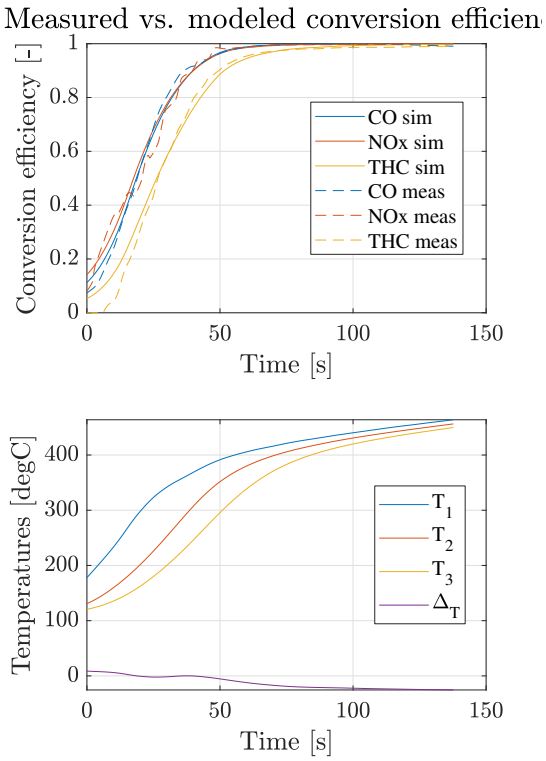

Figure 10: Simulated and measured output emissions. The core temperature of each axial slice T_1, T_2, T_3 as well as Δ_T is shown.

estimated parameters are shown in Table 5, and our estimated values of E_a are on the same order of magnitude (±50–100%) as those found in earlier studies, e.g. [23]. Note that we can not practically expect a more precise match as we do not model mass transport limitations, stored oxygen in the catalyst, and lambda-switching, all of which influence the apparent reaction kinetics.

Thermal dynamics parameters

The thermal dynamics tuning parameters τ_{ax}, τ_{ra}, τ_{amb}, k_{conv}, and τ_{convect} were also estimated using the cold-start thermal evolution. First, we set the initial state vector $\bar{T}(0) = [T_1, T_2, T_3, \Delta T]$ to the temperatures measured by Ts12a, Ts12b, Ts12c, and Ts10b − Ts12b respectively. Then, for given tuning parameter values we computed the modeled thermal evolution $\bar{T}(k)$, using an explicit 4'th order Runge-Kutta method. As the tuning parameter's influence on $\bar{T}(k)$ involves non-linear dynamics, conventional optimization methods tend to behave poorly. Here, we have used MATLAB's genetic algorithm (`ga`) tool, with the fitness function

$$\min \sum_k |\bar{T}(k) - \bar{T}_{\text{meas}}(k)|^2, \tag{36}$$

where $\bar{T}_{\text{meas}}$ is the measured temperature evolution at the sampled times (i.e. Ts12a, Ts12b, Ts12c, Ts10b − Ts12b), and otherwise using the default `ga` solver settings. Though other optimization methods tend to converge more quickly, the genetic algorithm is convenient in that it searches a wide range of initial values and the presented model evaluates quickly enough for the slow rate of convergence to not be problematic. Here, generating a solution required approximately 4 hours on a standard desktop PC (AMD Ryzen 2700x with 16 gb 3200 MHz RAM), where each model call required approximately 30 ms of compute time and generated modeled data corresponding to 425 seconds at sample rate of 50 ms (i.e. ≈ 280 000 model calls per second, or ≈ 15 000 times faster than realtime). The results gave good matching between the measured and simulated thermal trajectories, as shown in Figure 11. We re-ran the algorithm 10 times, and received virtually identical results each time.

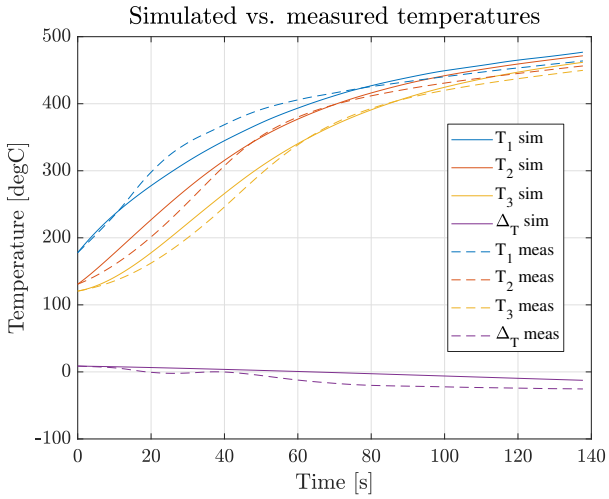

Figure 11: Simulated and measured thermal evolution of the TWC.

Table 5: Estimated reaction rate parameters.

Species	E_A [J/mol]	A
CO	$40.7 \cdot 10^3$	$161 \cdot 10^3$
NO_x	$37.5 \cdot 10^3$	$86.0 \cdot 10^3$
THC	$44.6 \cdot 10^3$	$215 \cdot 10^3$

Table 6: Estimated thermal parameters.

Parameter	Value
τ_{ax}	$88.2 \cdot 10^3$
τ_{ra}	385
τ_{amb}	$2.18 \cdot 10^3$
k_{conv}	$34.5 \cdot 10^{-6}$
τ_{convect}	171

The estimated parameters are listed in Table 6.

The difference between the measured and simulated temperatures in Figure 11 are typically within ±10°C, with a maximal deviation of 20°C. We hypothesize that the deviation between the simulated and measured T_1 at 20–60 seconds is caused by exhaust species that were adsorbed on the TWC during the first 20 seconds that start reacting as the TWC reaches lightoff (≈ 300°C). We have chosen not to model adsorbed exhaust species as this would require at least one additional state variable.

We can note that the thermal TWC model captures convective gas terms (seen during the first 20 seconds, where the entire TWC is below the light-off temperature) as well as exothermic reaction power generated in the TWC (seen after the first 80 seconds, where the TWC is well above the light-off temperature and is hotter than the incoming gasses). Furthermore, the model captures the characteristic thermal front that progresses from the front to the rear, as well as a radial temperature gradient that increases with increasing core temperatures, motivating our choice of a model that is axially and radially resolved.

Note that unlike many black-box modeling approaches, the tuning parameters in the model correspond to physical parameters. We hypothesize that this implies that we can tune the model for a given axial resolution M, and then easily generate tuning parameters for a different axial resolution M', by scaling the slice-volume-dependent parameters A and τ_{ax} by M/M', and using the remaining parameters as-is. However, we have as of yet not conclusively validated this hypothesis.

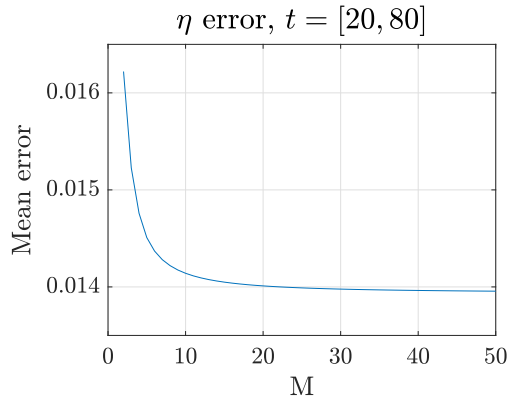

(a)

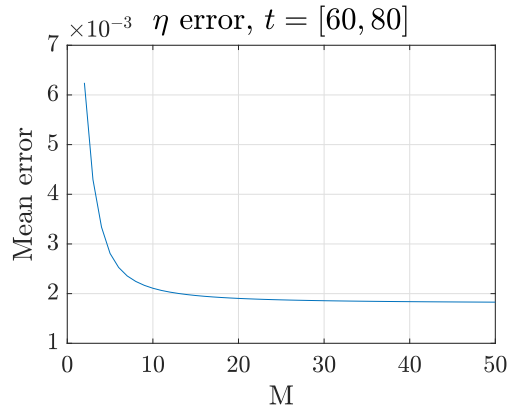

(b)

Figure 12: Mean absolute deviation between predicted and measured conversion efficiency for varying M. In Figure 12a this is computed over $t = [20, 80]$ s, while Figure 12b focuses on the region $t = [60, 80]$ s where Δ_T is more significant, as seen in Figure 10.

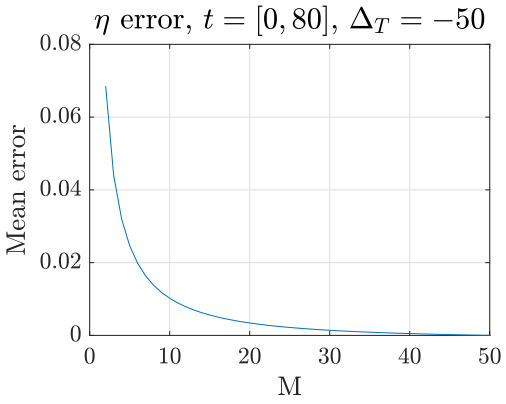

(a)

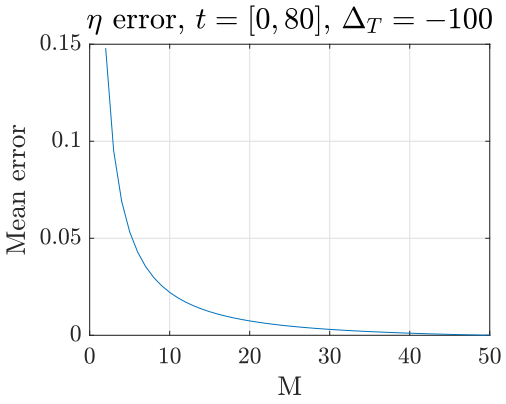

(b)

Figure 13: Mean absolute deviation between the simulated emission for $M = 50$ and the simulated emission for varying M, with Δ_T fixed to -50 and -100°C.

Radial resolution

One of the primary contributions of this paper is the inclusion of a radially resolved temperature profile. However, in order for this addition to be motivated, this should result in a model that more accurately predicts the TWC behavior. In Figure 12 we illustrate the mean deviation between the modeled and measured conversion efficiency (as previously studied in Figure 10) for varying radial resolutions M. Here, we have swept $M = [1, 50]$ while keeping the reaction rate parameters fixed at the values found for $M = 15$ (see Table 5). Both figures show an improvement in the estimated conversion efficiency with increasing M, indicating that resolving the radial temperature profile improves the model performance. Furthermore, the figures also indicate that the model is not over-fitted, as the prediction improves when M is increased from the value we used to tune the model. Finally, we can note that our choice of $M = 15$ is plausible, as the majority of the gains are had for $M \gtrsim 7$.

More specifically, if we consider Figure 12a, we can state that resolving the radial temperature profile marginally improves the average predicted conversion efficiency over $t = [20, 80]$, with a maximal relative improvement of approximately 15%. However, if we consult Figure 10 it is clear that $|\Delta_T|$ is very small at times $t = [20, 60]$. Limiting the averaging window to times where $|\Delta_T|$ is larger, e.g. $t = [60, 80]$, gives Figure 12b, where we see a relative improvement of approximately 350%. Though this is a very large relative improvement in accuracy, the absolute deviation between the modeled and measured conversion efficiency is small for all tested M here, as the conversion efficiency is very close to 1. However, had the engine been run in a manner that gave a large $|\Delta_T|$ near light-off we can expect the inclusion of a radially resolved temperature profile to give a significant absolute accuracy improvement. An illustration of this is shown in Figure 13, where we simulate the effect of a constant $\Delta_T = \{-50, -100\}$, but otherwise use the same thermal evolution and engine-out emissions. Though a constant Δ_T is not practically representative, it is plausible for $|\Delta_T|$ to be large during intervals near light-off. (For example, if a hybrid vehicle starts the combustion engine when reaching highway speeds the TWC periphery will be significantly cooled by the passing air.) In these figures we compare the mean emissions for $M = 50$ with the emissions for varying M over the entire cold-start phase. These results show that resolving the radial temperature distribution can lead to an average absolute accuracy improvement by 7–15 percentage points over the entire cold-start cycle, with gains that increase as the magnitude of Δ_T increases.

Conclusion

In this paper we have introduced a physics-based TWC model that resolves axial and radial thermal dynamics, while simultaneously keeping the number of state variables low, ultimately allowing for use as a model for fast off-line simulation or on-line control methods (e.g. nonlinear state-feedback methods and explicit MPC). The number of axial slices (and thereby the number of state variables) and radial resolution is configurable, allowing for balancing the computational demand and accuracy for a specific application. The model uses a first-principles approach for chemical kinetics, exothermic reaction power, gas convection, axial and radial thermal conduction, and an interpolation method for increasing the radial resolution.

Resolving the axial and radial temperature profile allows for implementing more nuanced control schemes, where if for instance during a cold-start the first axial slice(s) of the TWC are hot, then the exhaust mass-flow can be kept sufficiently low in order to increase the residence time in the hot part(s) of the TWC. This awareness of the TWC's condition is lost with most conventional on-line models that only characterize TWC temperature as a scalar value.

We have performed an experimental campaign where we measured the temperatures and emission massflow in the TWC using a conventional experimental rig. This experimental campaign required only a few hours of effective measurements, after which we were able to identify the model's tuning parameters. These consist of three activation energies, three pre-exponential scaling terms, one radial thermal distribution table, and five thermal parameters.

Subsequent analysis showed that the modeled and experimentally measured conversion efficiencies very closely match each other, even with only three axial slices. Furthermore, the modeled temperature evolution matched the experimentally measured temperature well, typically deviating no more than ±10°C. The most significant discrepancies were seen just after lightoff, plausibly due to exhaust species that adsorbed onto the cold TWC that then exothermically reacted after lightoff. Resolving the radial temperature profile improved the relative accuracy of conversion efficiency by approximately 15%, but would likely be much more significant for operating regimes with a more prominent radial temperature gradient. Simulations show the potential for the *absolute* conversion efficiency accuracy to improve by 7–15 percentage points when the temperature of the TWC periphery differs from the center by 100°C.

The fast computational speed of the model (approximately 15000 times faster than realtime on a desktop PC (AMD Ryzen 2700x with 16 gb 3200 MHz RAM) with unoptimized code) and the low number of state variables open up for several possible use-cases. Examples include closed-loop on-line control methods suited for low-dimensional non-linear models (such as nonlinear state-feedback and explicit MPC) and very numerically fast off-line TWC simulations. This can ultimately allow for on-line optimal cold-start strategies, TWC sizing, or more quickly evaluating the performance of exhaust aftertreatment systems with several different TWC elements. Relevant future work includes constructing a suitable state observer for on-line applications that have a limited number of measured temperatures.

References

1. J. B. Heywood, *Internal Combustion Engine Fundamentals*. McGraw Hill, 1988.

2. R. Hedinger, P. Elbert, and C. Onder, "Optimal Cold-Start Control of a Gasoline Engine," *Energies*, vol. 10, p. 1548, Oct. 2017.

3. K. Ramanathan, D. H. West, and V. Balakotaiah, "Optimal design of catalytic converters for minimizing cold-start emissions," *Catalysis Today*, vol. 98, no. 3, pp. 357–373, 2004.

4. J. Gao, G. Tian, A. Sorniotti, A. E. Karci, and R. Di Palo, "Review of thermal management of catalytic converters to decrease engine emissions during cold start and warm up," *Applied Thermal Engineering*, vol. 147, pp. 177–187, 2019.

5. M. Schori, T. Boehme, T. Jeinsch, and M. Schultalbers, "Optimal catalytic converter heating in hybrid vehicles," *SAE Technical Paper*, 2014.

6. R. S. Pannag, "Coldstart Modeling and Optimal Control Design for Automotive SI engine," 2009.

7. G. Fiengo, L. Glielmo, S. Santini, and G. Serra, "Control of the exhaust gas emissions during the warm-up process of a TWC-equipped SI engine," *IFAC Proceedings Volumes*, vol. 35, no. 1, pp. 301–306, 2002.

8. F. Keynejad and C. Manzie, "Suboptimal Cold Start Strategies for Spark Ignition Engines," *IEEE Transactions on Control Systems Technology*, vol. 21, pp. 1295–1308, July 2013.

9. D. Kum, H. Peng, and N. Bucknor, "Modeling and Control of Hybrid Electric Vehicles for Fuel and Emission Reduction," in

ASME 2008 Dynamic Systems and Control Conference, Parts A and B, (Ann Arbor, Michigan, USA), pp. 553–560, ASMEDC, Jan. 2008.

10. G. Fiengo, L. Glielmo, S. Santini, and G. Serra, "Control oriented models for TWC-equipped spark ignition engines during the warm-up phase," in *Proceedings of the 2002 American Control Conference (IEEE Cat. No.CH37301)*, (Anchorage, AK, USA), pp. 1761–1766 vol.3, IEEE, 2002.

11. E. Brandt, Yanying Wang, and J. Grizzle, "Dynamic modeling of a three-way catalyst for SI engine exhaust emission control," *IEEE Transactions on Control Systems Technology*, vol. 8, pp. 767–776, Sept. 2000.

12. U. Kiencke and L. Nielsen, *Automotive Control Systems*. Springer, 2000.

13. H. Bauer, ed., *Gasoline-engine management*. Robert Bosch GmbH, 1999.

14. P. Michel, "Optimizing fuel consumption and pollutant emissions of gasoline-HEV with catalytic converter," *Control Engineering Practice*, p. 8, 2017.

15. N. L. Azad, P. R. Sanketi, and J. K. Hedrick, "Determining Model Accuracy Requirements for Automotive Engine Coldstart Hydrocarbon Emissions Control," *Journal of Dynamic Systems, Measurement, and Control*, vol. 134, p. 051002, Sept. 2012.

16. Z. Zhu, S. Midlam-Mohler, and M. Canova, "Development of physics-based three-way catalytic converter model for real-time distributed temperature prediction using proper orthogonal decomposition and collocation," *International Journal of Engine Research*, p. 146808741987612, Sept. 2019.

17. D. P. Bertsekas, *Dynamic Programming and Optimal Control*, vol. 1. Athena Scientific, 4 ed., 2017.

18. M. L. Puterman, *Markov Decision Processes: Discrete Stochastic Dynamic Programming*. John Wiley & Sons, 1994.

19. J. Logan, F. Gehring, and P. Halmos, *Applied Partial Differential Equations*. Springer Undergraduate Mathematics Series, Springer, 1998.

20. K. N. Pattas, A. M. Stamatelos, P. K. Pistikopoulos, G. C. Koltsakis, P. A. Konstandinidis, E. Volpi, and E. Leveroni, "Transient modeling of 3-way catalytic converters," *International Congress & Exposition*, 1994.

21. S. Tischer, Y. Jiang, K. W. Hughes, M. D. Patil, and M. Murtagh, "Three-way-catalyst modeling - a comparison of 1d and 2d simulations," *SAE World Congress & Exhibition*, pp. 2007–01–1071, 2007.

22. I. Svraka and Ö. W. Linus, "Model based catalyst control," Master's thesis, Linköping University, 2019.

23. S. B. Kang, S. J. Han, I.-S. Nam, B. K. Cho, C. H. Kim, and S. H. Oh, "Detailed reaction kinetics for double-layered pd/rh bimetallic TWC monolith catalyst," *Chemical Engineering Journal*, vol. 241, pp. 273–287, 2014.

Nomenclature

TWC	Three way catalyst
DP	Dynamic programming
SI	Spark-ignited
DOHC	Dual Over Head Camshaft
CO	Carbon monoxide
$\mathrm{NO_x}$	Nitrogen oxides
THC	Total hydrocarbons
$\bar{T}$	Model state vector
T_n	Temperature of axial slice n
Δ_T	Temperature difference between radial center and radial periphery
N	Number of axial elements
M	Number of interpolated radial elements
$T_{n,m}$	Temperature of cell n, m
$\dot{m}_{n,m}$	Total massflow into cell n, m
$k^s_{n,m}$	Reaction rate of emission species s in cell n, m
A^s	Apparent pre-exponential scaling factor for Arrhenius expression for emission species s in any given cell
E^s_a	Activation energy for emission species s
$y^s_{n,m}$	Mole fraction of emission species s in cell n, m
t_r	Residence time of exhaust gas in a given cell
V_{slice}	Gas volume of each axial slice
V_{TWC}	Gas volume of the entire TWC
ν	Volumetric flow rate in a given cell
$\dot{m}_{\text{eng ex}}$	Total exhaust massflow
P	Absolute pressure in the TWC
$\dot{m}^{s,\text{out}}_{n,m}$	Massflow of emission species s leaving cell n, m
$\dot{m}^{s,\text{in}}_{n,m}$	Massflow of emission species s entering cell n, m
$\dot{m}^{s,\text{conv}}_{n,m}$	Massflow of emission species s converted in cell n, m
$\eta^s_{n,m}$	Conversion efficiency of emission species s in cell n, m
$\dot{m}^s_{\text{tp}}$	Tailpipe massflow of emission species s
$\mathrm{d}H_x$	Molar heat of reaction of x
$P_{n,m}$	Exothermic reaction power in cell n, m
$\bar{T}_{\text{cond}}$	State derivative due to conductive terms
$\bar{T}_{\text{exo}}$	State derivative due to exothermic reaction terms
$\bar{T}_{\text{convect}}$	State derivative due to convective terms
τ_{ax}	Tuning parameter, axial thermal resistance
τ_{ra}	Tuning parameter, radial thermal resistance
τ_{amb}	Tuning parameter, ambient thermal resistance
T_{amb}	Ambient temperature
$P_{\text{ctr,n}}$	Weighted exothermic reaction power, center of axial slice n
$P_{\text{per,n}}$	Weighted exothermic reaction power, periphery of axial slice n
k_{conv}	Tuning parameter, exothermic reaction power proportionality constant
τ_{convect}	Tuning parameter, gas convection proportionality constant
$T_{\text{eng ex}}$	Engine exhaust temperature
$\bar{T}_{\text{meas}}$	Experimentally measured temperatures corresponding to model state vector
t_{mid}	Relative radially midway temperature
$\dot{m}^s_{\text{tp,meas}}$	Experimentally measured tailpipe massflow of emission species s

Contact Information

Jonathan Lock
+46317725792
lock@chalmers.se

Acknowledgments

This work has been performed within the Combustion Engine Research Center at Chalmers (CERC) with financial support from the Swedish Energy Agency.